ACS APPLIED MATERIALS & INTERFACES

www.acsami.org

Research Article

Highly Sensitive, Stretchable, and Robust Strain Sensor Based on Crack Propagation and Opening

Shuang Wu, Katherine Moody, Abhiroop Kollipara, and Yong Zhu*

Cite This: *ACS Appl. Mater. Interfaces* 2023, 15, 1798−1807

Read Online

ACCESS | Metrics & More | Article Recommendations | Supporting Information

ABSTRACT: Soft and stretchable strain sensors have been attracting significant attention. However, the trade-off between the sensitivity (gauge factor) and the sensing range has been a major challenge. In this work, we report a soft stretchable resistive strain sensor with an unusual combination of high sensitivity, large sensing range, and high robustness. The sensor is made of a silver nanowire network embedded below the surface of an elastomeric matrix (e.g., poly(dimethylsiloxane)). Periodic mechanical cuts are applied to the top surface of the sensor, changing the current flow from uniformly across the sensor to along the conducting path defined by the open cracks. Both experiment and finite element analysis are conducted to study the effect of the slit depth, slit length, and pitch between the slits. The stretchable strain sensor can be integrated into wearable systems for monitoring physiological functions and body motions associated with different levels of strain, such as blood pressure and lower back health. Finally, a soft three-dimensional (3D) touch sensor that tracks both normal and shear stresses is developed for human−machine interfaces and tactile sensing for robotics.

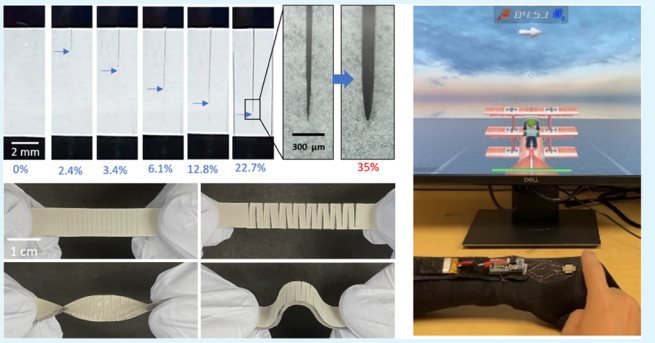

KEYWORDS: *strain sensor, silver nanowires, crack, stretchable electronics, health monitoring, human−machine interface*

INTRODUCTION

Soft and stretchable strain sensors have been attracting significant interest because of their wide applications in wearable electronics for physiological monitoring and motion tracking,[1−12] human−machine interfaces,[13−16] and soft robotics.[17−21] A variety of nanocomposite materials have been explored for use in soft and stretchable sensors, including carbon nanotubes (CNTs),[22−24] graphene,[25−27] metal nanoparticles,[28] magnetic nanoparticles,[29−33] and metal nanowires.[10,34−37] In stretchable strain sensors, these materials typically exist in the form of a three-dimensional percolation network embedded in a polymer matrix. Stretching the composite matrix decreases the percolation density, resulting in decreased electrical conductivity. In parallel, structural design strategies have been used to significantly reduce the effective strain on the conducting materials, leading to better stretchability. A number of mechanically guided structural designs have been reported, such as wrinkles,[38,39] serpentines,[40] spirals/helices,[41,42] kirigami,[43,44] and auxetic metamaterials.[45]

Recent advancements in wearable technology and soft robotics have led to the development of new stretchable strain sensors with enhanced sensing performances, such as large gauge factor (GF), large strain range, high linearity, better conformability, and robustness.[3] However, trade-offs between these performances have been a major challenge for almost all existing strain sensors. For example, a Pt/polyurethane acrylate (PUA) composite resistive sensor with surface crack design has been reported with an ultrahigh GF of 2000, yet a strain range of only 2%,[46] which is low for most applications such as body motion tracking. Another crack-based strain sensor also shows good sensitivity (GF = 9400) but with a small sensing range (<3%).[20] These examples illustrate the promising potential of measuring contact resistance change between crack surfaces for strain sensing. However, using well-defined, periodic mechanical cuts in soft materials to control crack propagation and opening has not been explored. On the other hand, a highly stretchable capacitive strain sensor enabled by wrinkled gold films showed a strain range of 250% but a GF of only 0.9,[47] which limits the sensing capabilities for small strains. Some researchers have also developed sensors with a large strain range (450−500%) and high sensitivity (GF of 67.7−10,000).[38,48] But they typically showed a nonlinear response (smaller GF at low strains and large GF at higher strains).

Received: September 16, 2022
Accepted: December 12, 2022
Published: December 22, 2022

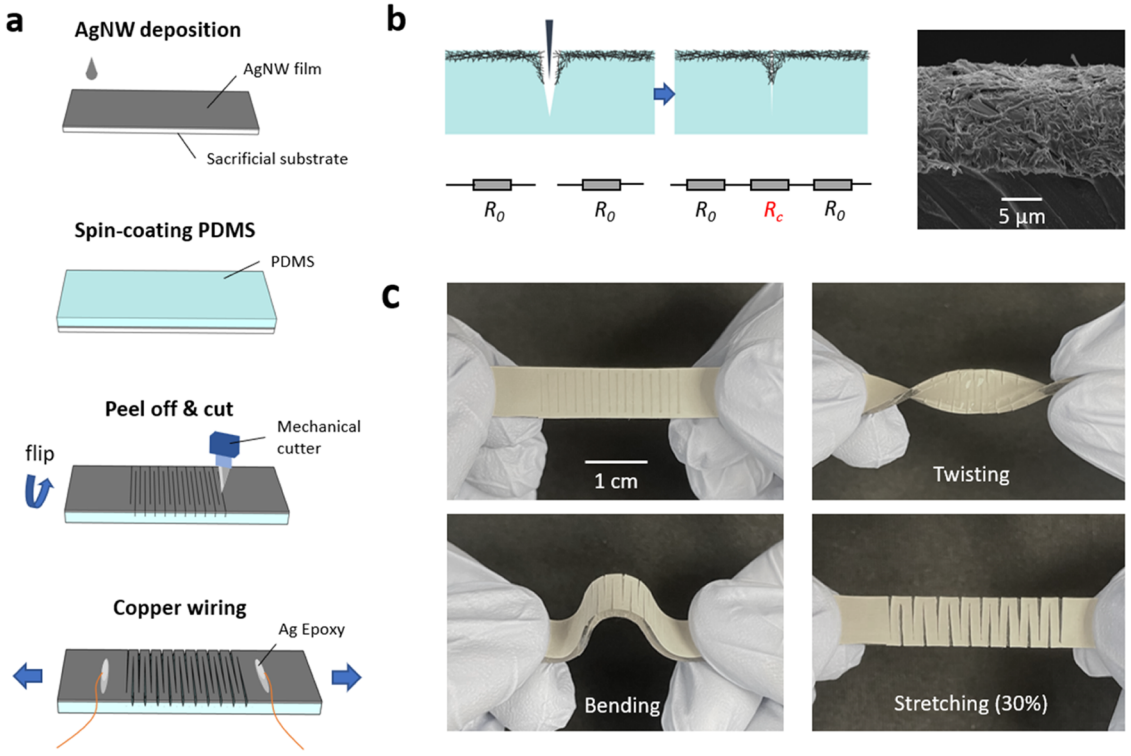

Figure 1. Overview of the soft stretchable strain sensor. (a) Fabrication process of the sensor. (b) Electrical model of the sensor during and after cuts. Scanning electron microscopy (SEM) image showing the cross-sectional view of one cut surface. (c) Undeformed sensor and the sensor under twisting, bending, and stretching.

For monitoring of human physiology and motion, the skin strain ranges from less than 1% to over 50%.[49] Typically, one sensor is used to detect subtle strains associated with physiological functions (e.g., blood pulse and respiration), while another is used for large strains associated with bending of body parts (e.g., knee, elbow, and back). It would be of great interest to develop one strain sensor, in the form of either a skin patch or a textile band, which can capture the full range of strains on human skin and can thus be attached onto different parts of the body.[50] For monitoring certain diseases, it is indeed critical to accurately measure a wide range of strains. For example, in the case of Parkinson's disease, the symptoms include resting tremor, rigid muscles, bradykinesia, and sometimes a combination of the above.[51−53] The sensors must be sensitive enough for monitoring small tremors while maintaining a large sensing range to measure joint movements. Moreover, soft strain sensors may encounter adverse conditions during operation, such as impacts and over-extension, where the applied strain could substantially exceed the sensing range. Therefore, it is of important relevance to develop a stretchable strain sensor with high sensitivity, large sensing range, and high robustness (i.e., surviving overstrain and repeatability), which remains a significant challenge.

This work reports a soft stretchable resistive strain sensor that can achieve all three goals by combining the use of nanomaterials with a novel structural design strategy. The sensor is made of a silver nanowire (AgNW) network embedded below the surface of poly(dimethylsiloxane) (PDMS). Periodic mechanical cuts are applied to the top surface of the AgNW/PDMS composite, changing the current flow from uniformly across the sensor to along the conducting path defined by the open cracks. Under the applied strain, the resistance increases as the crack propagates but remains constant as the crack reaches the cut length and exhibits tip blunting. Both regions are totally reversible and repeatable. Both experiment and finite element analysis have been conducted to study the effect of the cut depth, cut length, and pitch between the cuts, highlighting excellent tunability of the GF, sensing range, and reversible range of the sensor. The stretchable strain sensor was integrated into two systems for wearable monitoring of blood pressure and lower back health, demonstrating the capabilities for small-strain and large-strain sensing, respectively. Finally, a soft three-dimensional (3D) touch sensor that tracks both normal and shear stresses was developed for human−machine interfaces and tactile sensing for robotics.

RESULTS

Figure 1a shows the fabrication process of the AgNW strain sensor with the surface crack design. The AgNW solution was drop-cast on a sacrificial substrate and then heated to evaporate the solvent. Then, liquid PDMS precursor was mixed thoroughly and spin-coated on top of the AgNW network. The AgNW/PDMS composite was cured at 70 °C for 1 h. The cured sample was then peeled off from the substrate with the AgNW network embedded below the surface of the PDMS matrix.[54] Then, the composite film was cut from the AgNW side using a mechanical cutter, cutting through the AgNW/PDMS composite into the pure PDMS layer (Figure 1b). The AgNW/PDMS layer was cut into a zigzag-shaped pattern. Finally, Cu lead wires were attached to the two ends of the pattern by silver epoxy.

Figure 1b shows the electrical models of the samples during and after the mechanical cuts. $2R_0$ is the initial resistance of the sample. As the razor blade cuts through the AgNW/PDMS composite, AgNWs along the cutting path are broken and

https://doi.org/10.1021/acsami.2c16741
ACS Appl. Mater. Interfaces 2023, 15, 1798−1807

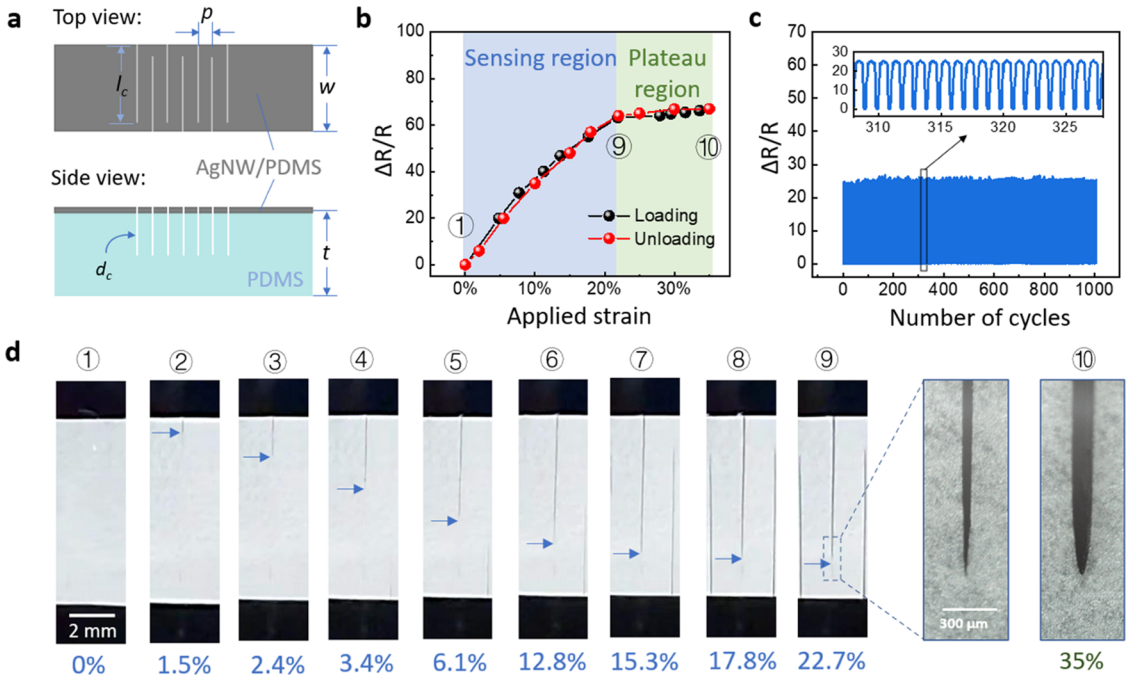

Figure 2. Electrical performances of the strain sensor under applied strain. (a) Schematic of the sensor showing the pitch between slits p, slit length l_c, specimen width w, slit depth d_c, and specimen thickness t. (b) Resistance change of the sensor corresponding to snapshots in (d). (c) Sensor response to 1000 cycles of 30% applied strain. The inset shows 20 cycles. (d) Snapshots of the top surface of the sensor under applied strain with magnified photographs showing the crack opening and tip blunting.

pushed in. After retrieval of the blade, the AgNWs on the two cutting surfaces form a physical contact with the contact resistance of R_c. The SEM image shows the cross-sectional view of the cutting surface.

Figure S1 shows the resistance changes of the AgNW/PDMS composite samples of different AgNW densities with respect to the number of slits. All samples showed a gradual increase in resistance with the increasing number of slits. The sample with a AgNW density of 0.5 mg/cm^2 yielded a minimum resistance change of only 15.3% after 5 cuts, while the sample with a AgNW density of 0.1 mg/cm^2 showed a resistance change of 321.9%. This can be explained by the different fracture mechanisms in the two cases. From Figure S2a, the low-density sample showed a clean-cut surface with AgNWs along the cutting path broken and sticking out. The depth of the conductive contact surface in this case was ~3 μm. However, for the sample with a high-density AgNW network, the AgNW/PDMS composite was deformed and pushed inward. In the case of 0.5 mg/cm^2, the depth of the conductive contact surface was over 13 μm (Figure S2b). This large contact area enabled the resistance change to be as low as 5% after each slit. In the rest of this work, 0.5 mg/cm^2 AgNW density was chosen for all of the strain sensors due to their stable contact resistances. The force−displacement curves of the samples with different AgNW densities are shown in Figure S3. It can be seen that a higher cutting force is required to break through the composite layer with a higher AgNW density. Figure 1c shows the crack-based strain sensor under twisting, bending, and stretching (30% strain). With the increase in the applied strain, the crack gradually propagated, which caused R_c to increase; inversely, with a decrease in the applied strain, the crack retracted, leading to a decrease in R_c. The electromechanical response of the sensor is highly reversible under cyclic loading (to be discussed in Figure 2).

To study the electrical performance of the sensors for different geometrical designs, we defined three major geometrical parameters—ratio of the slit depth to the sample thickness d_c/t, ratio of the pitch between the slits to the specimen width p/w, and ratio of the slit length to the specimen width l_c/w (Figure 2a). Figure 2b shows the resistance change of the crack-based sensor as a function of the applied strain. The resistance change curve can be divided into two regions, a sensing region where the resistance increases linearly with the increasing strain, and a plateau region. The crack propagation/opening process was observed in situ under an optical microscope, while the resistance was measured simultaneously. 1000 stretching/unloading cycles (1.2 mm/s) were applied to show the excellent repeatability of the sensor for long-term use (Figure 2c). Figure S4 shows the resistance change and the stress of the sensor, measured concurrently, under cyclic loading at different strain rates (1.2, 0.6, and 0.3 mm/s), which shows good repeatability in all cases.

The optical images in the sensing range (Figure 2d ①—⑨) show the gradual propagation of a single crack. In this range, the current flow follows the slit-guided path. As a result, the resistance of the sensor increases with the crack propagating. However, this resistance change stops when the crack is fully open, i.e., the two crack surfaces lose contact, as shown in the magnified optical image (Figure 2d, ⑩). Figure S5 also shows the relationship between the applied strain, the crack length, and the relative resistance change.

The sensor can be further stretched without resistance change, as shown in the plateau region in Figure 2b. In this case, the crack reaches the full slit length. Under the applied strain, the crack further opens with the crack tip blunting but not advancing beyond the slit length. This plateau region is important as it can protect the sensors from failing due to

https://doi.org/10.1021/acsami.2c16741
ACS Appl. Mater. Interfaces 2023, 15, 1798−1807

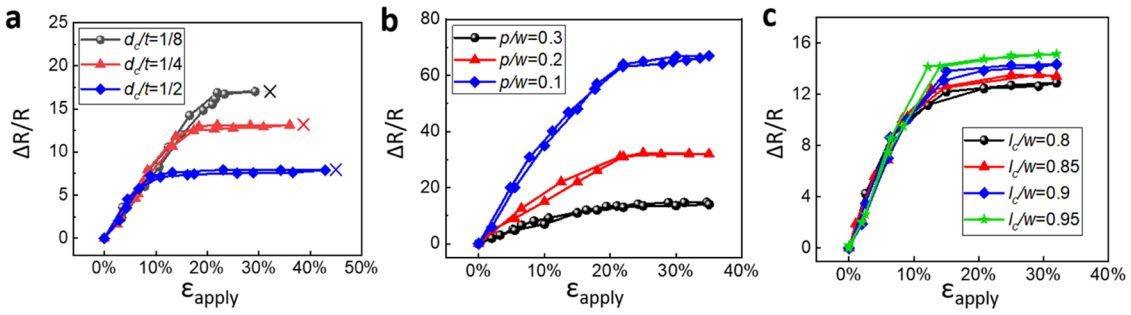

Figure 3. Geometrical design of the strain sensor. (a) Resistance change of the sensors with d_c/t = 1/8, 1/4, and 1/2 with respect to applied strain. Three cross markers with corresponding color represent the reversible range of each case from FEA. (b) Resistance change of the sensors with p/w = 0.1, 0.2, and 0.3 with respect to applied strain. (c) Resistance change of the sensors with l_c/w = 0.8, 0.85, 0.9, and 0.95 with respect to applied strain.

unexpected large strains. Here we define this reversible range by the combination of the sensing region and the plateau region. Beyond the plateau region, the local strain in front of the crack tip would cause irreversible sliding in the AgNW network, leading to overall irreversible resistance change. If the applied strain further increases, the crack tip could propagate beyond the slit length, causing more serious irreversibility in the resistance.

Figure 3a shows the relative resistance changes of three samples with d_c/t of 1/8, 1/4, and 1/2, with p, w, and l_c remaining the same (p/w = 0.2, l_c/w = 0.9). The three cases showed the same GF of 81.5 and the linear sensing region gradually increased with the decreasing slit depth. This is due to the difference in the crack propagation rate for the different slit depths. The shallower the slits, the larger the applied strain to complete the crack propagation and opening. The plateau region gradually decreased with the decreasing slit depth (Figure 2d).

In Figure S6, finite element analysis (FEA) (ABAQUS, version 2017) was conducted to simulate the crack propagation and opening behavior of the AgNW/PDMS composite. With the introduction of mechanical cuts, the effective modulus reduces. With larger d_c/t, the effective modulus reduces more. Similarly, with smaller p/w and larger l_c/w, the effective modulus drop of the sensor increases (Figure S7). The maximum strain in the AgNW/PDMS layer lies ahead of the crack tip during stretching. When it exceeds a critical strain ε_c, we assume that the irreversible sliding in the AgNW network occurs, causing irreversible damage in the AgNW network and hence the irreversible resistance of the sensor. The critical strain on AgNW/PDMS composite was measured to be ε_c = 5% under tension. As shown in Figure S8, the resistance of the AgNW beyond 5% tensile strain was irreversible. Here, we characterize the reversible range by the applied strain when the maximum strain at the crack tip of the AgNW/PDMS layer reaches 5%. FEA simulations found the reversible ranges of 31.4, 38.3, and 45.1% for d_c/t of 1/8, 1/4, and 1/2, respectively (marked with cross marks in Figure 3a). To guarantee the reversibility of the sensor, the applied strain remains below the reversible range, which is much smaller than the breaking strain; above the breaking strain, the crack would further advance beyond the initial slit length. To sum up, with different slit depths, a trade-off exists between the sensing range and the reversible range while having the same GF.

Figure 3b demonstrates the effect of p/w on the relative resistance change, while d_c/t and l_c/w remained at 1/8 and 0.9, respectively. With the decrease of p/w from 0.3 to 0.1, the GF increased from 81.5 to 290.1. With a smaller p/w, the pitch between the slits decreases while the total length of the conducting path increases, thus the overall resistance change can increase dramatically. Figure 3c shows a slight increase of the resistance change with the increasing l_c/w while keeping d_c/t = 1/8 and p/w = 0.3 because the final "neck" of the conducting path after the crack propagation completes is narrower with the increase of l_c/w. These results on the three parameters, d_c/t, p/w, and l_c/w, demonstrated excellent tunability of the GF, sensing range, and reversible range of the sensor.

Figure 4 shows a benchmark comparison between the present work and the reported stretchable strain sensors

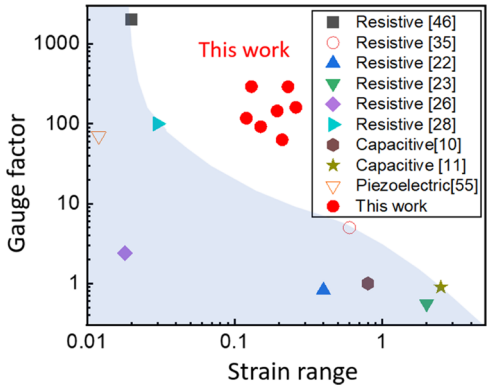

Figure 4. Performances of the strain sensors compared with the reported stretchable strain sensors.

enabled by different sensing mechanisms, including resistive sensors[22,23,26,28,35,46] capacitive sensors,[10,11] and piezoelectric sensors.[55] Of note is that the selected strain sensors in the map all showed high linearity and reversibility. In general, a trade-off exists between the GF and the sensing range for stretchable strain sensors. From this map, it can be seen that the present work yields a large GF = 290.1 with a decent strain sensing range (22%), exceeding the envelop defined by the reported stretchable strain sensors. After integration on stretchable substrates (e.g., athletic tape to be discussed later), the stretchability of the sensor can be further enhanced.

A coupled electromechanical FEA model was built (COMSOL Multiphysics 5.6) to understand the resistance change of the strain sensor under stretching (Figure S9a). The AgNW/PDMS composite was modeled as an isotropic conductive material and the contact resistance between the

https://doi.org/10.1021/acsami.2c16741
ACS Appl. Mater. Interfaces 2023, 15, 1798−1807

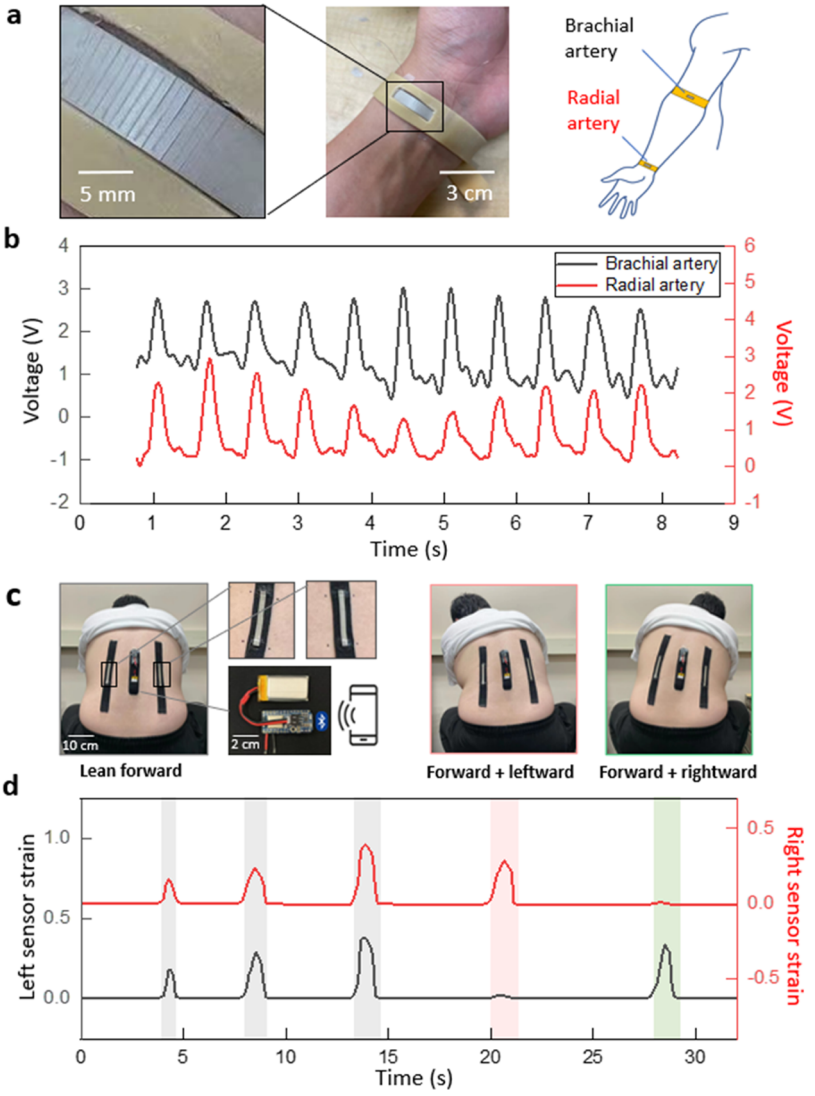

Figure 5. Demonstrations of the strain sensor for personal health monitoring. (a) Sensor integrated with a wristband for monitoring blood pulse. (b) Sensing results of two blood pulse sensors placed on the radial artery on the wrist and the brachial artery on the arm. (c) Photographs of the sensor integrated with an athletic tape attached side by side along the spine for monitoring lower back strains. The inset shows the two sensors and the Bluetooth evaluation board for data collection and transmission. (d) Sensing results of the two-sensor system detecting different bending motions of the lower back corresponding to photographs in (c).

two crack surfaces was considered to be dependent on the crack opening. When the distance between the two surfaces exceeds a critical value, the contact resistance drops from an initial value to zero. This model can simulate the gradual propagation and opening of the crack. Material parameters used in the simulation such as sheet resistance of the AgNW/PDMS composite and contact resistance were measured (e.g., in the case of NW density of 0.5 mg/cm^2, the sheet resistance of the AgNW/PDMS composite is 0.25 Ω/sq and the contact resistance per unit length is 1.6 Ω/cm). By taking the integral of the ECD along the conducting path we can calculate the resistance change with respect to the applied strain. The FEA results agreed well with the experimental results of different p/w ratios (Figure S9b). Figure S9c shows the simulated electrical current density (ECD) field of the strain sensor before and after stretching. With the increase of the applied strain, the ECD field shows a transition from uniform current flow (across the closed cracks) to current flow along the conducting path defined by the open cracks. This model could predict the performance of the sensors with even more complicated cutting patterns, providing valuable guidance to the sensor design.

To demonstrate the versatile applicability of our strain sensors for monitoring human motions, we first applied the sensors on the wrist to detect the pulse wave, which represents one of the most delicate strain signals on human skin. Figure 5a shows the setup consisting of a rubber band with a slot filled with the strain sensor. The rubber band was fastened on the wrist to secure the strain sensor against the pulsing area. When the blood pumps through the vein, the two ends of the strain sensor are fixed by the rubber band while the middle is bent and stretched. Then, the cracks are opened on the top surface. The red curve in Figure 5b shows the pulse wave captured from the radial artery on the wrist. Similarly, another strain sensor can be placed on the brachial artery on the arm, recording another pulse wave simultaneously (black curve in Figure 5b). By measuring the distance between the two pulse areas and taking the average of the time gap between peaks of

https://doi.org/10.1021/acsami.2c16741
ACS Appl. Mater. Interfaces 2023, 15, 1798−1807

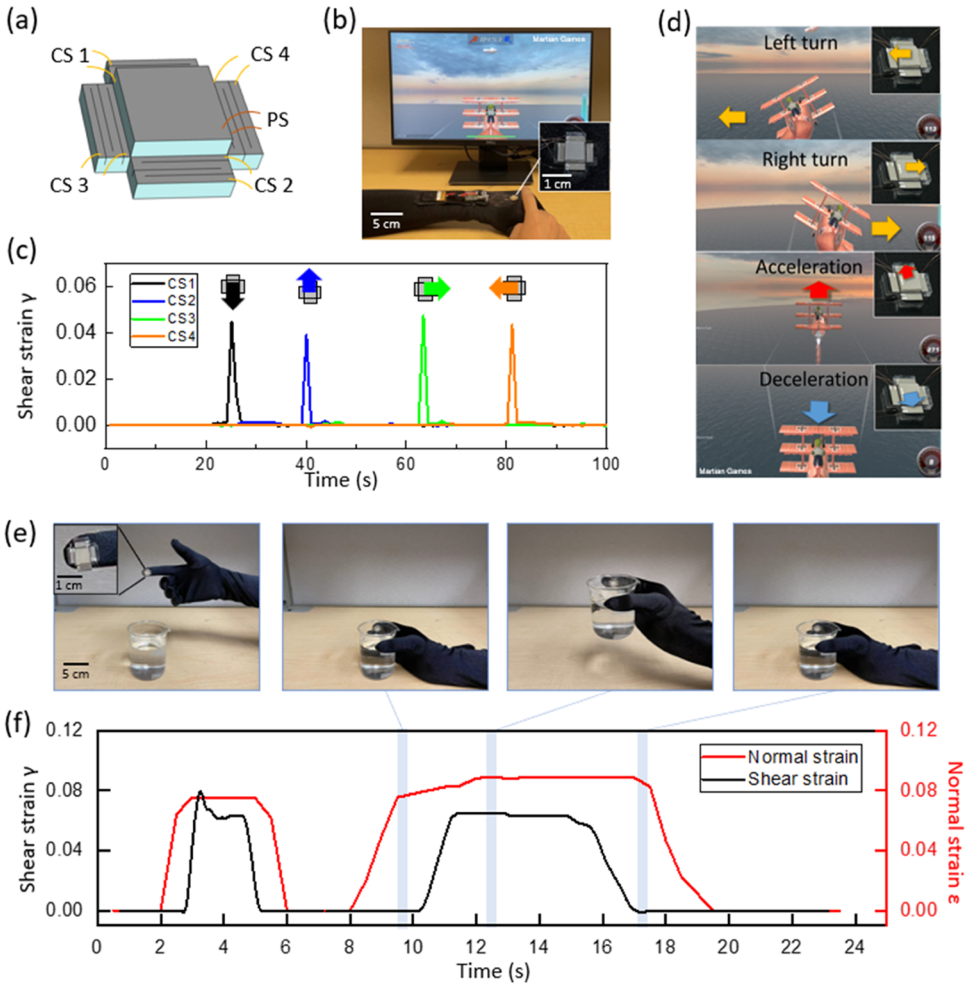

Figure 6. Demonstration of the strain sensor for human−machine interface and tactile sensing. (a) Schematic layout of the 3D touch sensor consisting of a capacitive normal strain sensor and four shear strain sensors. (b) Photograph of the 3D touch sensor connected to an evaluation board and laptop. The inset shows the 3D touch sensor. (c) Shear strain of the touch sensor when pushing toward different directions using a finger. (d) Application in playing an airplane video game. The four sensors correspond to four different functions: turning left, turning down, acceleration, and deceleration. (e) Snapshots showing different stages of grasping a glass of water including grabbing, lifting, and dropping. (f) Shear strain and normal strain of the tactile sensor during two trials of grasping of the cup of water, showing the grabbing, lifting, and dropping.

the two pulse waves, the averaged pulse wave velocity (PWV) can be measured, based on which the blood pressure (BP) can be obtained following[56]

$$\mathrm{BP} = \alpha \mathrm{PWV}^2 + \beta$$

where α = 0.18 kPa·s^2·m^{-2} and β = 2.7 kPa.[56] Taking PWV = 7.5 m/s as measured from Figure 5b, the BP was calculated to be 12.8 kPa, which equals 96.2 mmHg.

The other demonstration aimed to monitor the large strains on the lower back, which is a critical signal for metabolic syndrome and spine issues.[57,58] The sensor was integrated onto an athletic tape by fixing the two ends of the sensor on the tape using a PDMS precursor (Figure 5c, inset). Two sensor/tape setups were attached on the lower back side by side in parallel with the spine. An Arduino Bluetooth board/tape was attached in the middle area of the lower back to collect and transmit the sensing signals to a smart phone. The details of the Bluetooth board design are shown in Figure S10, where R_0 is the dummy resistor and R_1−R_6 are the six available channels (only two used in this demonstration). The subject started from a sitting-straight posture and leaned forward three times with increasing degree. Then, the subject leaned forward while tilting rightward and leftward. Figure 5c shows the measured strain signals of the two sensor/tape setups. When leaning forward, both sensors responded with resistance increases. While leaning forward and tilted sideways, the resistance of the sensor on the corresponding side remained nearly constant and the one on opposite side increased substantially. The calibration of the sensor/fabric setup is shown in Figure S11a. Four fiducial markers were drawn alongside the crack-based sensors on the skin for the purpose of validation. The results measured by the sensor and by the fiducial markers showed excellent agreement (Figure S11b). Of note is that by integrating the strain sensor with a stretchable athletic tape, the overall stretchability of the sensor/tape setup can be increased on demand according to the need of the applications. In the setup, the strain distributions in the sensor/tape region and the pure tape are different. Due to the larger Young's modulus, the sensor/tape region has a smaller strain than the pure tape region. By adjusting the modulus ratio, a sensor/tape setup can be easily integrated for wearable applications with large stretchability, e.g., motion tracking on human joints.

Finally, besides wearable personal health monitoring, the sensor can be applied for human−machine interfaces and

https://doi.org/10.1021/acsami.2c16741
ACS Appl. Mater. Interfaces 2023, 15, 1798−1807

robotics. Figure 6a shows the schematic diagram of an integrated 3D touch sensor. The two solid AgNW/PDMS composite in the middle form a capacitive pressure sensor that detects normal pressure,[8] while the four surrounding AgNW/PDMS composite ribbons with the surface crack design (CS1, CS2, CS3, and CS4) work as shear stress sensors. The pressure sensor was connected to a capacitance evaluation board and the shear sensors were connected to a multichannel resistance meter (Figure 6b). Figure S12 shows the calibration results of the shear sensors. When a shear force is applied in the middle area, one shear stress sensor away from the moving direction is stretched. The cracks in the stretched sensor open, resulting in a resistance increase. Figure 6c shows excellent decoupled responses when shear forces in four directions were applied sequentially. Figure 6d shows real-time control of an airplane in a video game with the functions of turning left, turning right, acceleration, and deceleration. This device illustrates a promising potential in virtual reality and soft human−machine interfaces.

Figure 6e shows the sensor applied for tactile sensing. The sensor was integrated on the fingertip of a glove and then used for grasping a glass of water (200 g). Figure 6f captures the shear and normal strains of two trials with different lifting and dropping speeds. When the glass of water was grabbed but not lifted, the capacitance of the middle sensor increased while the resistance of the shear sensor remained constant. During lifting, the shear strain increased to overcome the gravity of the glass of water. When dropping the water on the table, the shear strain decreased to zero followed by the normal strain decreasing to zero. Note that the shear strain curve of the first trial showed a period of overshot because the fast lifting required extra shear force for acceleration. However, the second trial was 3 times slower in the lifting speed and the shear strain showed no obvious overshot. This application demonstrated the great potential for tactile sensing for robotics.

CONCLUSIONS

In summary, this work reported simple, facile fabrication of a versatile soft stretchable strain sensor based on resistive sensing for wearable applications. We designed and fabricated a AgNW/PDMS composite-based strain sensor with simple mechanical cuts into the top surface. Under the applied strain, the resistance increased as the crack propagated (the sensing range) but remained constant as the crack reached the slit length (the reversible range). Under further loading, the local strain in front of the crack tip would cause irreversible sliding in the AgNW network, leading to irreversible resistance change. The effects of the slit depth, slit length, and pitch between the slits were studied to optimize the sensor performances. This sensor overcame the limitation of most existing strain sensors and offered unprecedented combination of GF, strain sensing range, and robustness (under overstrain and 1000 repeated loading cycles). A large GF of 290.1 was achieved with a sensing range over 22%. FEA was conducted to validate the electrical performance and predict the mechanical damage, agreeing very well with the experimental results. As demonstrations, the stretchable strain sensor was integrated into several systems for wearable monitoring of blood pressure and lower back health and 3D touch sensing that tracks both compressive and shear stresses simultaneously, illustrating the promising potential for a range of applications including personal human health monitoring, human−machine interfaces, and tactile sensing for robotics.

METHODS

Synthesis of AgNW Solution. First, 60 mL of a 0.147 M PVP (MW ∼ 40,000, Sigma-Aldrich) solution in EG was added to a flask, to which a stir bar was added; the solution was then suspended in an oil bath (temperature 151.5 °C) and heated for 1 h under magnetic stirring (150 rpm). Then, 200 μL of a 24 M $CuCl_2$ ($CuCl_2{\cdot}2H_2O$, >99.999%, Sigma-Aldrich) solution in EG was injected into the PVP solution. The mixture solution was then injected with 60 mL of a 0.094 M $AgNO_3$ (>99%, Sigma-Aldrich) solution in EG.[59]

Fabrication of the Strain Sensor. The AgNW solution was drop-cast on a plasma-treated glass slide, which was placed onto a hot plate at 50 °C to evaporate the solvent. After the solvent was evaporated, liquid PDMS (SYLGARD 184, DOW, Inc.) with a weight ratio of 10:1 was mixed thoroughly and dropped on top of the AgNW film in a rectangular mold. The AgNW/PDMS composite was cured at 70 °C for 1 h.[10,60] The cured sample was then cut from the top surface using a mechanical cutter (silhouette CAMEO). Cu wires were attached to the two outer ends of the sample by silver epoxy (MG Chemicals).

Fabrication of the 3D Touch Sensor. First, the as-synthesized AgNWs were drop-cast onto a sacrificial substrate. The AgNWs together with the sacrificial substrate were then laser cut into a cross-shaped pattern. The pattern defined the conductive area into five regions: a square region in the middle (one electrode of the capacitive sensor) and four surrounding rectangular regions (for making the crack-based resistive strain sensors). PDMS was poured on top of the five pieces of AgNWs and then baked at 70 °C for 1 h. After curing of PDMS, the sample was flipped over and cut on the designed areas using the mechanical cuter. Another piece of AgNW/PDMS composite was glued on top of the middle square region to compose a capacitive pressure sensor. Then, all five parts of the touch sensor were wired with copper wires.

Video Game Control Using the 3D Touch Sensor. To transmit the resistance signal, we used an ARDUINO board (nano 33) and built a simple voltage divider circuit with four dummy resistors. Each channel of the touch sensor was connected to a dummy resistor in series. The voltages across dummy resistors and crack sensors were collected by the ARDUINO board and processed to calculate the real-time resistances of the sensors in each direction. An ARDUINO code was built to read the real-time resistance values of each channel and compare them to a triggering threshold *Rt* to decide whether or not to send out a signal. For example, when the 3D touch sensor was pressed and pushed to the right direction, the left crack sensor CS3 reached a resistance increase of over 20% which triggered the ARDUINO board to send out a keyboard signal "right arrow." As a result, the airplane in the video game will make a right turn. Similarly, the other three crack-based sensors have been assigned to "left arrow," "up arrow," and "down arrow." In the airplane video game, the four arrow keys represent the functions of turning left, turning right, acceleration, and deceleration.

ASSOCIATED CONTENT

Supporting Information

The Supporting Information is available free of charge at https://pubs.acs.org/doi/10.1021/acsami.2c16741.

Resistance change of AgNW/PDMS composites with an increase in the number of cuts; SEM images of the cut surfaces of AgNW/PDMS composite with AgNW densities of 0.1 and 0.5 mg/cm^2; force−displacement curves of a razor blade pushing into the AgNW/PDMS composites of different AgNW densities; electromechanical simulation of the strain sensor: schematic plot of the sensor, electrical current densities of the sensor at zero and 15% strain, comparison between FEA and

https://doi.org/10.1021/acsami.2c16741
ACS Appl. Mater. Interfaces 2023, 15, 1798−1807

experimental results of the sensor with p/w = 0.1, 0.2, and 0.3; crack length with respect to applied strain; relative resistance changes with respect to crack length; FEA simulation of the strain distribution of the sensor under 30% applied strain; resistance changes of the AgNW/PDMS composite under 5% and 6% stretching and unloading; photograph of the Arduino Bluetooth board for the wearable strain sensing system (with custom-made voltage divider circuit); diagram showing the design of the Bluetooth board and voltage divider circuit; calibration of the sensors integrated with athletic fabrics; photographs of the sensor/fabric setup with fiducial marker dots on the skin; comparison between the strains measured by the sensor/fabric and by the fiducial markers using a camera; calibration of the shear strain sensor enabled by two sensors; photograph of a shear strain sensing system with two orthogonal strain sensors; and resistance change of the sensors in the horizontal direction and vertical direction with a vertical shear strain applied (PDF)

Real-time control of an airplane in a video game with the functions of turning left, turning right, acceleration, and deceleration (Movie 1) (MP4)

Robotic sensing of grabbing, lifting, and dropping a glass of water (Movie 2) (MP4)

AUTHOR INFORMATION

Corresponding Author

Yong Zhu − *Department of Mechanical and Aerospace Engineering, North Carolina State University, Raleigh, North Carolina 27695, United States; Department of Materials Science and Engineering, North Carolina State University, Raleigh, North Carolina 27695, United States; Joint Department of Biomedical Engineering, University of North Carolina-Chapel Hill and NC State University, Chapel Hill, North Carolina 27599, United States;* orcid.org/0000-0002-3862-5757; Email: yzhu7@ncsu.edu

Authors

Shuang Wu − *Department of Mechanical and Aerospace Engineering, North Carolina State University, Raleigh, North Carolina 27695, United States;* orcid.org/0000-0003-2579-9309

Katherine Moody − *Department of Mechanical and Aerospace Engineering, North Carolina State University, Raleigh, North Carolina 27695, United States*

Abhiroop Kollipara − *Department of Mechanical and Aerospace Engineering, North Carolina State University, Raleigh, North Carolina 27695, United States*

Complete contact information is available at: https://pubs.acs.org/10.1021/acsami.2c16741

Author Contributions

S.W. and Y.Z. conceived the idea and designed the experiments and simulations. S.W. conducted the experiments, simulations, and data analysis. K.M. helped with the data analysis. A.K. helped with the electronics for data acquisition. S.W. and Y.Z. wrote the manuscript with inputs from all of the authors.

Notes

The authors declare no competing financial interest.

ACKNOWLEDGMENTS

The authors gratefully acknowledge the financial support from NSF (award no. 2122841), NIH (award no. R01HD108473), and DOD (award no. W81XWH-21-1-0185).

REFERENCES

(1) Lipomi, D. J.; Vosgueritchian, M.; Tee, B. C.; Hellstrom, S. L.; Lee, J. A.; Fox, C. H.; Bao, Z. Skin-Like Pressure and Strain Sensors Based on Transparent Elastic Films of Carbon Nanotubes. *Nat. Nanotechnol.* **2011**, *6*, 788−792.

(2) Chung, H. U.; Rwei, A. Y.; Hourlier-Fargette, A.; Xu, S.; Lee, K.; Dunne, E. C.; Xie, Z.; Liu, C.; Carlini, A.; Kim, D. H.; Ryu, D.; Kulikova, E.; Cao, J.; Odland, I. C.; Fields, K. B.; Hopkins, B.; Banks, A.; Ogle, C.; Grande, D.; Park, J. B.; Kim, J.; Irie, M.; Jang, H.; Lee, J.; Park, Y.; Kim, J.; Jo, H. H.; Hahm, H.; Avila, R.; Xu, Y.; Namkoong, M.; Kwak, J. W.; Suen, E.; Paulus, M. A.; Kim, R. J.; Parsons, B. V.; Human, K. A.; Kim, S. S.; Patel, M.; Reuther, W.; Kim, H. S.; Lee, S. H.; Leedle, J. D.; Yun, Y.; Rigali, S.; Son, T.; Jung, I.; Arafa, H.; Soundararajan, V. R.; Ollech, A.; Shukla, A.; Bradley, A.; Schau, M.; Rand, C. M.; Marsillio, L. E.; Harris, Z. L.; Huang, Y.; Hamvas, A.; Paller, A. S.; Weese-Mayer, D. E.; Lee, J. Y.; Rogers, J. A. Skin-Interfaced Biosensors for Advanced Wireless Physiological Monitoring in Neonatal and Pediatric Intensive-Care Units. *Nat. Med.* **2020**, *26*, 418−429.

(3) Amjadi, M.; Kyung, K. U.; Park, I.; Sitti, M. Stretchable, Skin-Mountable, and Wearable Strain Sensors and Their Potential Applications: A Review. *Adv. Funct. Mater.* **2016**, *26*, 1678−1698.

(4) Kim, D.-H.; Lu, N.; Ma, R.; Kim, Y.-S.; Kim, R.-H.; Wang, S.; Wu, J.; Won, S. M.; Tao, H.; Islam, A.; Yu, K. J.; Kim, T.-i.; Chowdhury, R.; Ying, M.; Xu, L.; Li, M.; Chung, H.-J.; Keum, H.; Mccormick, M.; Liu, P.; Zhang, Y.; Omenetto, F. G.; Huang, Yg.; Coleman, T.; Rogers, J. A. Epidermal Electronics. *Science* **2011**, *333*, 838−843.

(5) Boutry, C. M.; Kaizawa, Y.; Schroeder, B. C.; Chortos, A.; Legrand, A.; Wang, Z.; Chang, J.; Fox, P.; Bao, Z. A Stretchable and Biodegradable Strain and Pressure Sensor for Orthopaedic Application. *Nat. Electron.* **2018**, *1*, 314−321.

(6) Libanori, A.; Chen, G.; Zhao, X.; Zhou, Y.; Chen, J. Smart Textiles for Personalized Healthcare. *Nat. Electron.* **2022**, *5*, 142−156.

(7) Zhou, Z.; Chen, K.; Li, X.; Zhang, S.; Wu, Y.; Zhou, Y.; Meng, K.; Sun, C.; He, Q.; Fan, W.; Fan, E.; Lin, Z.; Tan, X.; Deng, W.; Yang, J.; Chen, J. Sign-to-Speech Translation Using Machine-Learning-Assisted Stretchable Sensor Arrays. *Nat. Electron.* **2020**, *3*, 571−578.

(8) Amjadi, M.; Pichitpajongkit, A.; Lee, S.; Ryu, S.; Park, I. Highly Stretchable and Sensitive Strain Sensor Based on Silver Nanowire−Elastomer Nanocomposite. *ACS Nano* **2014**, *8*, 5154−5163.

(9) Cai, G.; Wang, J.; Qian, K.; Chen, J.; Li, S.; Lee, P. S. Extremely Stretchable Strain Sensors Based on Conductive Self-Healing Dynamic Cross-Links Hydrogels for Human-Motion Detection. *Adv. Sci.* **2017**, *4*, No. 1600190.

(10) Yao, S.; Zhu, Y. Wearable Multifunctional Sensors Using Printed Stretchable Conductors Made of Silver Nanowires. *Nanoscale* **2014**, *6*, 2345−2352.

(11) Yao, S.; Vargas, L.; Hu, X.; Zhu, Y. A Novel Finger Kinematic Tracking Method Based on Skin-Like Wearable Strain Sensors. *IEEE Sens. J.* **2018**, *18*, 3010−3015.

(12) Yao, S.; Ren, P.; Song, R.; Liu, Y.; Huang, Q.; Dong, J.; O'Connor, B. T.; Zhu, Y. Nanomaterial-Enabled Flexible and Stretchable Sensing Systems: Processing, Integration, and Applications. *Adv. Mater.* **2020**, *32*, No. 1902343.

(13) Yu, Y.; Nassar, J.; Xu, C.; Min, J.; Yang, Y.; Dai, A.; Doshi, R.; Huang, A.; Song, Y.; Gehlhar, R.; et al. Biofuel-Powered Soft Electronic Skin with Multiplexed and Wireless Sensing for Human-Machine Interfaces. *Sci. Rob.* **2020**, *5*, No. eaaz7946.

(14) Wang, K.; Yap, L. W.; Gong, S.; Wang, R.; Wang, S. J.; Cheng, W. Nanowire-Based Soft Wearable Human−Machine Interfaces for

Future Virtual and Augmented Reality Applications. *Adv. Funct. Mater.* **2021**, No. 2008347.
(15) Jeong, J.-W.; Yeo, W.-H.; Akhtar, A.; Norton, J. J. S.; Kwack, Y.-J.; Li, S.; Jung, S.-Y.; Su, Y.; Lee, W.; Xia, J.; Cheng, H.; Huang, Y.; Choi, W.-S.; Bretl, T.; Rogers, J. A. Materials and Optimized Designs for Human-Machine Interfaces Via Epidermal Electronics. *Adv. Mater.* **2013**, *25*, 6839−6846.
(16) Zhou, W.; Yao, S.; Wang, H.; Du, Q.; Ma, Y.; Zhu, Y. Gas-Permeable, Ultrathin, Stretchable Epidermal Electronics with Porous Electrodes. *ACS Nano* **2020**, *14*, 5798−5805.
(17) Lu, N.; Kim, D.-H. Flexible and Stretchable Electronics Paving the Way for Soft Robotics. *Soft Rob.* **2014**, *1*, 53−62.
(18) Rich, S. I.; Wood, R. J.; Majidi, C. Untethered Soft Robotics. *Nat. Electron* **2018**, *1*, 102−112.
(19) Thuruthel, T. G.; Shih, B.; Laschi, C.; Tolley, M. T. Soft Robot Perception Using Embedded Soft Sensors and Recurrent Neural Networks. *Sci. Rob.* **2019**, *4*, No. eaav1488.
(20) Araromi, O. A.; Graule, M. A.; Dorsey, K. L.; Castellanos, S.; Foster, J. R.; Hsu, W.-H.; Passy, A. E.; Vlassak, J. J.; Weaver, J. C.; Walsh, C. J.; Wood, R. J. Ultra-Sensitive and Resilient Compliant Strain Gauges for Soft Machines. *Nature* **2020**, *587*, 219−224.
(21) Wu, S.; Baker, G. L.; Yin, J.; Zhu, Y. Fast Thermal Actuators for Soft Robotics. *Soft Rob.* **2021**, 1031−1039.
(22) Yamada, T.; Hayamizu, Y.; Yamamoto, Y.; Yomogida, Y.; Izadi-Najafabadi, A.; Futaba, D. N.; Hata, K. A Stretchable Carbon Nanotube Strain Sensor for Human-Motion Detection. *Nat. Nanotechnol.* **2011**, *6*, 296−301.
(23) Ryu, S.; Lee, P.; Chou, J. B.; Xu, R.; Zhao, R.; Hart, A. J.; Kim, S.-G. Extremely Elastic Wearable Carbon Nanotube Fiber Strain Sensor for Monitoring of Human Motion. *ACS Nano* **2015**, *9*, 5929−5936.
(24) Zhu, S.; Sun, H.; Lu, Y.; Wang, S.; Yue, Y.; Xu, X.; Mei, C.; Xiao, H.; Fu, Q.; Han, J. Inherently Conductive Poly (Dimethylsiloxane) Elastomers Synergistically Mediated by Nanocellulose/Carbon Nanotube Nanohybrids toward Highly Sensitive, Stretchable, and Durable Strain Sensors. *ACS Appl. Mater. Interfaces* **2021**, *13*, 59142−59153.
(25) Yu, X.; Cheng, H.; Zhang, M.; Zhao, Y.; Qu, L.; Shi, G. Graphene-Based Smart Materials. *Nat. Rev. Mater.* **2017**, *2*, No. 17046.
(26) Bae, S.-H.; Lee, Y.; Sharma, B. K.; Lee, H.-J.; Kim, J.-H.; Ahn, J.-H. Graphene-Based Transparent Strain Sensor. *Carbon* **2013**, *51*, 236−242.
(27) Iqra, M.; Anwar, F.; Jan, R.; Mohammad, M. A. A Flexible Piezoresistive Strain Sensor Based on Laser Scribed Graphene Oxide on Polydimethylsiloxane. *Sci. Rep.* **2022**, *12*, No. 4882.
(28) Zheng, M.; Li, W.; Xu, M.; Xu, N.; Chen, P.; Han, M.; Xie, B. Strain Sensors Based on Chromium Nanoparticle Arrays. *Nanoscale* **2014**, *6*, 3930−3933.
(29) Zhou, Y.; Zhao, X.; Xu, J.; Fang, Y.; Chen, G.; Song, Y.; Li, S.; Chen, J. Giant Magnetoelastic Effect in Soft Systems for Bioelectronics. *Nat. Mater.* **2021**, *20*, 1670−1676.
(30) Zhao, X.; Zhou, Y.; Xu, J.; Chen, G.; Fang, Y.; Tat, T.; Xiao, X.; Song, Y.; Li, S.; Chen, J. Soft Fibers with Magnetoelasticity for Wearable Electronics. *Nat. Commun.* **2021**, *12*, No. 6755.
(31) Chen, G.; Zhao, X.; Andalib, S.; Xu, J.; Zhou, Y.; Tat, T.; Lin, K.; Chen, J. Discovering Giant Magnetoelasticity in Soft Matter for Electronic Textiles. *Matter* **2021**, *4*, 3725−3740.
(32) Zhao, X.; Chen, G.; Zhou, Y.; Nashalian, A.; Xu, J.; Tat, T.; Song, Y.; Libanori, A.; Xu, S.; Li, S.; Chen, J. Giant Magnetoelastic Effect Enabled Stretchable Sensor for Self-Powered Biomonitoring. *ACS Nano* **2022**, *16*, 6013−6022.
(33) Xu, J.; Tat, T.; Zhao, X.; Zhou, Y.; Ngo, D.; Xiao, X.; Chen, J. A Programmable Magnetoelastic Sensor Array for Self-Powered Human−Machine Interface. *Appl. Phys. Rev.* **2022**, *9*, No. 031404.
(34) Yao, S.; Zhu, Y. Nanomaterial-Enabled Stretchable Conductors: Strategies, Materials and Devices. *Adv. Mater.* **2015**, *27*, 1480−1511.
(35) Ho, M. D.; Ling, Y.; Yap, L. W.; Wang, Y.; Dong, D.; Zhao, Y.; Cheng, W. Percolating Network of Ultrathin Gold Nanowires and Silver Nanowires toward "Invisible" Wearable Sensors for Detecting Emotional Expression and Apexcardiogram. *Adv. Funct. Mater.* **2017**, *27*, No. 1700845.
(36) Yao, S.; Yang, J.; Poblete, F. R.; Hu, X.; Zhu, Y. Multifunctional Electronic Textiles Using Silver Nanowire Composites. *ACS Appl. Mater. Interfaces* **2019**, *11*, 31028−31037.
(37) Kim, K. K.; Hong, S.; Cho, H. M.; Lee, J.; Suh, Y. D.; Ham, J.; Ko, S. H. Highly Sensitive and Stretchable Multidimensional Strain Sensor with Prestrained Anisotropic Metal Nanowire Percolation Networks. *Nano Lett.* **2015**, *15*, 5240−5247.
(38) Huang, J.; Zhou, J.; Luo, Y.; Yan, G.; Liu, Y.; Shen, Y.; Xu, Y.; Li, H.; Yan, L.; Zhang, G.; et al. Wrinkle-Enabled Highly Stretchable Strain Sensors for Wide-Range Health Monitoring with a Big Data Cloud Platform. *ACS Appl. Mater. Interfaces* **2020**, *12*, 43009−43017.
(39) Sun, H.; Dai, K.; Zhai, W.; Zhou, Y.; Li, J.; Zheng, G.; Li, B.; Liu, C.; Shen, C. A Highly Sensitive and Stretchable Yarn Strain Sensor for Human Motion Tracking Utilizing a Wrinkle-Assisted Crack Structure. *ACS Appl. Mater. Interfaces* **2019**, *11*, 36052−36062.
(40) Yan, Z.; Pan, T.; Wang, D.; Li, J.; Jin, L.; Huang, L.; Jiang, J.; Qi, Z.; Zhang, H.; Gao, M.; et al. Stretchable Micromotion Sensor with Enhanced Sensitivity Using Serpentine Layout. *ACS Appl. Mater. Interfaces* **2019**, *11*, 12261−12271.
(41) Gao, Y.; Guo, F.; Cao, P.; Liu, J.; Li, D.; Wu, J.; Wang, N.; Su, Y.; Zhao, Y. Winding-Locked Carbon Nanotubes/Polymer Nanofibers Helical Yarn for Ultrastretchable Conductor and Strain Sensor. *ACS Nano* **2020**, *14*, 3442−3450.
(42) Li, C.; Cui, Y.-L.; Tian, G.-L.; Shu, Y.; Wang, X.-F.; Tian, H.; Yang, Y.; Wei, F.; Ren, T.-L. Flexible Cnt-Array Double Helices Strain Sensor with High Stretchability for Motion Capture. *Sci. Rep.* **2015**, *5*, No. 15554.
(43) Sun, R.; Zhang, B.; Yang, L.; Zhang, W.; Farrow, I.; Scarpa, F.; Rossiter, J. Kirigami Stretchable Strain Sensors with Enhanced Piezoelectricity Induced by Topological Electrodes. *Appl. Phys. Lett.* **2018**, *112*, No. 251904.
(44) Wu, C.; Wang, X.; Lin, L.; Guo, H.; Wang, Z. L. Based Triboelectric Nanogenerators Made of Stretchable Interlocking Kirigami Patterns. *ACS Nano* **2016**, *10*, 4652−4659.
(45) Jiang, Y.; Liu, Z.; Matsuhisa, N.; Qi, D.; Leow, W. R.; Yang, H.; Yu, J.; Chen, G.; Liu, Y.; Wan, C.; Liu, Z.; Chen, X. Auxetic Mechanical Metamaterials to Enhance Sensitivity of Stretchable Strain Sensors. *Adv. Mater.* **2018**, *30*, No. 1706589.
(46) Kang, D.; Pikhitsa, P. V.; Choi, Y. W.; Lee, C.; Shin, S. S.; Piao, L.; Park, B.; Suh, K.-Y.; Kim, T.-i.; Choi, M. Ultrasensitive Mechanical Crack-Based Sensor Inspired by the Spider Sensory System. *Nature* **2014**, *516*, 222−226.
(47) Atalay, O.; Atalay, A.; Gafford, J.; Wang, H.; Wood, R.; Walsh, C. A Highly Stretchable Capacitive-Based Strain Sensor Based on Metal Deposition and Laser Rastering. *Adv. Mater. Technol.* **2017**, *2*, No. 1700081.
(48) Lee, J.; Shin, S.; Lee, S.; Song, J.; Kang, S.; Han, H.; Kim, S.; Kim, S.; Seo, J.; Kim, D.; Lee, T. Highly Sensitive Multifilament Fiber Strain Sensors with Ultrabroad Sensing Range for Textile Electronics. *ACS Nano* **2018**, *12*, 4259−4268.
(49) Jeong, Y. R.; Park, H.; Jin, S. W.; Hong, S. Y.; Lee, S. S.; Ha, J. S. Highly Stretchable and Sensitive Strain Sensors Using Fragmentized Graphene Foam. *Adv. Funct. Mater.* **2015**, *25*, 4228−4236.
(50) Shi, C.; Zou, Z.; Lei, Z.; Zhu, P.; Nie, G.; Zhang, W.; Xiao, J. Stretchable, Rehealable, Recyclable, and Reconfigurable Integrated Strain Sensor for Joint Motion and Respiration Monitoring. *Research* **2021**, *2021*, No. 9846036.
(51) Dorsey, E. R.; Bloem, B. R. The Parkinson Pandemic—a Call to Action. *JAMA Neurol.* **2018**, *75*, 9−10.
(52) Monje, M. H.; Foffani, G.; Obeso, J.; Sánchez-Ferro, Á. New Sensor and Wearable Technologies to Aid in the Diagnosis and Treatment Monitoring of Parkinson's Disease. *Ann. Rev. Biomed. Eng.* **2019**, *21*, 111−143.
(53) Deuschl, G.; Krack, P.; Lauk, M.; Timmer, J. Clinical Neurophysiology of Tremor. *J. Clin. Neurophysiol.* **1996**, *13*, 110−121.

https://doi.org/10.1021/acsami.2c16741
ACS Appl. Mater. Interfaces 2023, 15, 1798−1807

(54) Xu, F.; Zhu, Y. Highly Conductive and Stretchable Silver Nanowire Conductors. *Adv. Mater.* **2012**, *24*, 5117−5122.
(55) Liao, Q.; Mohr, M.; Zhang, X.; Zhang, Z.; Zhang, Y.; Fecht, H.-J. Carbon Fiber−Zno Nanowire Hybrid Structures for Flexible and Adaptable Strain Sensors. *Nanoscale* **2013**, *5*, 12350−12355.
(56) Ma, Y.; Choi, J.; Hourlier-Fargette, A.; Xue, Y.; Chung, H. U.; Lee, J. Y.; Wang, X.; Xie, Z.; Kang, D.; Wang, H.; Han, S.; Kang, S.-K.; Kang, Y.; Yu, X.; Slepian, M. J.; Raj, M. S.; Model, J. B.; Feng, X.; Ghaffari, R.; Rogers, J. A.; Huang, Y. Relation between Blood Pressure and Pulse Wave Velocity for Human Arteries. *Proc. Natl. Acad. Sci. U.S.A.* **2018**, *115*, 11144−11149.
(57) Roy, S. H.; De Luca, C. J.; Casavant, D. A. Lumbar Muscle Fatigue and Chronic Lower Back Pain. *Spine* **1989**, *14*, 992−1001.
(58) Dankaerts, W.; O'Sullivan, P.; Burnett, A.; Straker, L. Differences in Sitting Postures Are Associated with Nonspecific Chronic Low Back Pain Disorders When Patients Are Subclassified. *Spine* **2006**, *31*, 698−704.
(59) Xia, Y.; Yang, P.; Sun, Y.; Wu, Y.; Mayers, B.; Gates, B.; Yin, Y.; Kim, F.; Yan, H. One-Dimensional Nanostructures: Synthesis, Characterization, and Applications. *Adv. Mater.* **2003**, *15*, 353−389.
(60) Yao, S.; Cui, J.; Cui, Z.; Zhu, Y. Soft Electrothermal Actuators Using Silver Nanowire Heaters. *Nanoscale* **2017**, *9*, 3797−3805.

https://doi.org/10.1021/acsami.2c16741
ACS Appl. Mater. Interfaces 2023, 15, 1798−1807